RESEARCH ARTICLE

Optimization, Green Synthesis, and Comprehensive Characterization of Silver Nanoparticles Using Plant Extracts

C.L. Sindhura[1], G'oFurjonov Mirzohid Mirzahparjon o'g'li[2], Jayanalina. T[3], K.K. Senthilkumar[4], D. Sudhahar[5], Ikramov Suxrobxon Saidmaxmud o'g'li[6], Ksenofontova Kristina Borisovna[7] and Varsha Deva[8*]

[1]*Narayana Pharmacy College, Nellore, Andhra Pradesh – 524003, India.*

[2]*Pediatrics-2 Department, Fergana Public Health Medical Institute, Yangi Turon 2A, Fergana - 150100, Uzbekistan.*

[3]*Department of Physics, Nandha Engineering College (Autonomous), Erode – 638052, Tamil Nadu, India.*

[4]*Department of Pharmaceutical Analysis, SS Institute of Pharmacy, Sankari, Salem, Tamil Nadu, India.*

[5]*Graphic Era Hill University, Bhimtal Campus, Sattal Mahara Gaon Road, Bhimtal, Nainital, Bhowali, Uttarakhand – 263132, India.*

[6]*Internal Medicine in Family Medicine, Central Asian Medical University, 150100, Burkhoniddin Margilanii Street 62a, Fergana, Uzbekistan.*

[7]*Doctor of Regional Multidisciplinary Medical Center, Fergana, Uzbekistan.*

[8]*Glocal University Pharmacy College, Glocal University, Saharanpur, India.*

***Corresponding Author**

Prof. (Dr.) Varsha Deva,

Principal,

Glocal University Pharmacy College, Glocal University,

Saharanpur.

E-mail: varsha.moon@gmail.com

Abstract

Green synthesis of silver nanoparticles (AgNPs) using plant-derived reducing agents offers a sustainable, non-toxic, and cost-effective alternative to conventional physicochemical fabrication methods. This study presents the systematic optimization, biogenic fabrication, and exhaustive physicochemical characterization of AgNPs synthesized using aqueous leaf extracts of Azadirachta indica (neem), Ocimum sanctum (tulsi), and Aloe vera as dual-function bioreductants and capping agents. Eight formulations (F1–F8) were designed by varying silver nitrate (AgNO3) concentration (1.0–2.0 mM), extract volume ratio (10–20% v/v), reaction pH (7–10), and temperature (25–80°C). Comprehensive characterization was performed using UV-Visible spectrophotometry, Fourier Transform Infrared Spectroscopy (FTIR), X-ray Diffraction (XRD), Dynamic Light Scattering (DLS), Transmission Electron Microscopy (TEM), Scanning Electron Microscopy coupled with Energy Dispersive X-ray Spectroscopy (SEM-EDX), Zeta potential analysis, Thermogravimetric Analysis (TGA), and Differential Scanning Calorimetry (DSC)1,2. The optimized formulation F5 (A. indica extract, 1.5 mM AgNO3, 15% v/v, pH 9, 60°C) yielded monodisperse, predominantly spherical AgNPs with a characteristic Surface Plasmon Resonance (SPR) peak at 428 nm, mean hydrodynamic diameter of 18.3 nm, polydispersity index (PDI) of 0.198, and zeta potential of −38.4 mV, indicative of excellent colloidal stability3. XRD confirmed face-centered cubic (FCC) crystallinity with a Scherrer crystallite size of 14.2 nm. FTIR analysis revealed phytochemical functional groups (hydroxyl, carbonyl, amine) involved in reduction and surface capping. Broad-spectrum antimicrobial evaluation demonstrated potent activity against Staphylococcus aureus, Escherichia coli, and fungal pathogens. Antioxidant (DPPH IC50 = 84.6 µg/mL) and photocatalytic degradation of methylene blue (91.4% efficiency, 120 min) further established the multifunctional utility of optimized AgNPs4,5. This investigation provides a robust, reproducible green synthesis platform applicable to pharmaceutical, biomedical, and environmental remediation contexts.

Keywords: Silver nanoparticles; Green synthesis; Azadirachta indica; Ocimum sanctum; Aloe vera; Characterization; Antimicrobial activity; Antioxidant; Surface plasmon resonance; Photocatalysis; Colloidal stability; Phytochemicals.

How to cite this article: Sindhura CL, Mirzohid Mirzahparjon O'G'Li G, Jayanalina T, Senthilkumar KK, Sudhahar D, Saidmaxmud O'G'Li IS, Borisovna KK, Deva V. Optimization, Green Synthesis, and Comprehensive Characterization of

Silver Nanoparticles Using Plant Extracts. Int J Drug Deliv Technol. 2026;16(19s): 420-435. DOI: 10.25258/ijddt.16.19s.51

1. Introduction

Nanotechnology has transformed modern material science by enabling the engineering of materials at the 1–100 nm scale, where quantum mechanical effects and dramatically altered physicochemical properties diverge substantially from bulk material behaviour[1]. Among the diverse library of metallic nanomaterials investigated globally, silver nanoparticles (AgNPs) occupy a privileged position due to their extraordinary broad-spectrum antimicrobial potency, size-tunable optical properties arising from Surface Plasmon Resonance (SPR), potent heterogeneous catalytic activity, and acceptable biocompatibility at physiologically relevant doses[2,3]. These characteristics have propelled AgNPs into numerous high-impact application domains including wound management dressings, antifouling coatings for medical implants, anti-biofilm textiles, water purification membranes, point-of-care diagnostic biosensors, targeted drug nanocarriers, and environmental pollutant degradation systems[4].

Conventional synthetic methodologies for AgNPs—encompassing chemical reduction using sodium borohydride or citrate, physical techniques such as laser ablation and electrochemical deposition, and gamma/UV radiation-assisted approaches—suffer from significant disadvantages that constrain their large-scale and biomedical deployment[5,6]. These include the generation of environmentally hazardous chemical by-products, the requirement for specialized and expensive instrumentation, high energy consumption, stringent inert atmosphere conditions, difficulties in achieving monodisperse size distributions, and compromised nanoparticle biocompatibility due to residual toxic stabilizing agents.

Green or biogenic synthesis—the fabrication of nanoparticles using biological entities including plant extracts, microbial cultures, algae, fungi, or biomass-derived molecules—has emerged as a scientifically compelling and industrially attractive alternative that intrinsically circumvents the drawbacks of conventional methods[7]. Plant extracts are particularly advantageous as they serve dual roles: their abundant phytochemicals (polyphenols, flavonoids, terpenoids, alkaloids, saponins, reducing sugars, and organic acids) act simultaneously as potent electron donors for reducing ionic silver (Ag^+) to zero-valent metallic silver (Ag^0), and as natural capping/stabilizing agents that adsorb onto nascent nanoparticle surfaces, imparting steric and electrostatic colloidal stabilization[8,9]. The entire process is typically conducted in aqueous media at ambient or mildly elevated temperatures, requires no inert atmosphere, and generates no hazardous chemical waste.

Azadirachta indica (neem), one of the most pharmacologically diverse medicinal trees of the Indian subcontinent, contains nimbin, nimbidin, azadirachtin, quercetin, rutin, kaempferol, and a rich suite of limonoids and terpenoids that collectively confer powerful antioxidant and antimicrobial properties and potent reducing capacity[10]. *Ocimum sanctum* (holy basil/tulsi), revered in traditional Ayurvedic medicine, is rich in eugenol, rosmarinic acid, ursolic acid, linalool, and apigenin, demonstrating excellent bioreductive potential for metal nanoparticle synthesis[11]. *Aloe vera* gel, widely exploited in cosmetic and pharmaceutical industries, contains acemannan polysaccharides, anthraquinones (barbaloin, aloesin), vitamins C and E, and abundant hydroxyl-bearing reducing sugars that are well-documented as effective bioreductants[12].

Despite the rapidly expanding literature on plant-mediated AgNP synthesis, critical gaps persist: most studies employ a single plant species without comparative optimization; characterization panels are frequently limited to UV-Vis and FTIR, omitting thermal analysis and elemental mapping; formal formulation design frameworks are rarely employed; and multi-functional biological evaluation within a unified experimental design is uncommonly reported[13,14]. The present study addresses these gaps comprehensively by: (i) employing three phytochemically distinct plant extracts; (ii) constructing a systematic formulation design of eight coded formulations varying four process parameters; (iii) conducting ten-technique exhaustive characterization; and (iv) evaluating antimicrobial, antifungal, antioxidant, and photocatalytic activities—providing a data-rich, reproducible platform for the translational development of green-synthesized AgNPs[15].

2. Materials

Silver nitrate ($AgNO_3$, ≥99.8% purity, MW 169.87 g/mol) was procured from Sigma-Aldrich (St. Louis, MO, USA) and served as the primary silver ion precursor. Sodium hydroxide (NaOH) and hydrochloric acid (HCl, 37% w/v), both analytical reagent (AR) grade, were obtained from HiMedia Laboratories Pvt. Ltd. (Mumbai, India) for pH adjustment. Analytical-grade ethanol (99.9%), methanol,

and dimethyl sulfoxide (DMSO) were sourced from Merck KGaA (Darmstadt, Germany). Microbiological culture media—Müller-Hinton agar, nutrient broth, potato dextrose agar, and Sabouraud dextrose agar—were supplied by HiMedia Laboratories[16]. DPPH (2,2-diphenyl-1-picrylhydrazyl) free radical reagent, ascorbic acid (positive antioxidant control), and methylene blue dye (photocatalytic substrate, MW 319.85 g/mol, purity ≥98%) were procured from Sigma-Aldrich. All solutions were prepared in Milli-Q ultrapure water (resistivity 18.2 MΩ·cm at 25°C, Millipore, Burlington, MA, USA) to eliminate ionic contamination .

Fresh, mature leaves of *Azadirachta indica* and *Ocimum sanctum*, and inner gel fillets of *Aloe vera*, were collected from the Medicinal Plant Garden, Department of Botany, University of Allahabad, Prayagraj, India. Plant material was taxonomically authenticated by a certified botanist, and voucher specimens were deposited in the institutional herbarium (Voucher nos.: AI/2024/007, OS/2024/008, AV/2024/009). All plant material was surface-washed under running tap water, rinsed three times with Milli-Q water, blotted dry with sterile filter paper, and shade-dried at ambient temperature (25°C) for 72 hours to remove surface moisture without thermal degradation of thermolabile phytoconstituents[17]. Extracts were prepared fresh before each synthesis batch and used within 48 hours to prevent microbial contamination and phytochemical oxidation.

Standard laboratory equipment utilized included: UV-Visible spectrophotometer (Shimadzu UV-1800, Kyoto, Japan), FTIR spectrometer with UATR accessory (PerkinElmer Spectrum Two, Waltham, MA, USA), X-ray diffractometer (Rigaku MiniFlex 600, Tokyo, Japan), DLS and zeta potential analyzer (Malvern Zetasizer Nano ZS, UK), TEM (JEOL JEM-2100, 200 kV, Tokyo, Japan), SEM-EDX (ZEISS EVO-18, Oberkochen, Germany), TGA (TA Instruments Q50, New Castle, USA), DSC (TA Instruments Q20, New Castle, USA), digital pH meter (Eutech pH 700, Thermo Fisher Scientific), refrigerated centrifuge (Eppendorf 5804R, Hamburg, Germany), freeze-dryer (Christ Alpha 1-2 LDplus, Osterode, Germany), and bench-top orbital incubator shaker (Thermo Scientific MaxQ 4000). All glassware was acid-washed in 10% v/v HNO3 solution, rinsed extensively with Milli-Q water, and oven-dried at 120°C prior to use to prevent metallic contamination[18].

3. Methods

3.1 Preparation of Aqueous Plant Extracts

Ten grams of fresh plant material (leaves or gel) were cut into approximately 0.5 cm pieces and boiled with 100 mL of Milli-Q water in a 250 mL borosilicate round-bottom flask at 60°C for 20 minutes with continuous magnetic stirring at 200 rpm. After cooling to room temperature, the extract was filtered sequentially through Whatman No. 1 (particle retention 11 µm), Whatman No. 42 (2.5 µm), and finally 0.22 µm syringe-tip membrane filters (Merck Millipore) to obtain particle-free sterile aqueous extract[18]. Extracts were stored at 4°C in amber glass vials**.**

3.2 Preliminary Phytochemical Screening

Qualitative phytochemical screening of all three plant extracts was conducted for the following classes of phytoconstituents: alkaloids (Dragendorff's and Wagner's reagents), flavonoids (alkaline reagent test with sodium hydroxide), tannins (1% ferric chloride test), terpenoids (Salkowski test with chloroform and concentrated H2SO4), saponins (foam test with vigorous shaking), phenolic compounds (lead acetate test), and reducing sugars (Fehling's test)[19]. Results were recorded as positive (+) or negative (−).

3.3 Quantitative Phytochemical Analysis

Total phenolic content (TPC) was determined by the Folin-Ciocalteu reagent method. Briefly, 0.5 mL of extract (1 mg/mL) was mixed with 2.5 mL of 10% Folin-Ciocalteu reagent and 2.0 mL of 7.5% sodium carbonate solution. After 30 minutes of incubation at 45°C, absorbance at 765 nm was measured and TPC expressed as mg gallic acid equivalents per gram (mg GAE/g) using a gallic acid calibration curve (10–100 µg/mL; $R^2 = 0.9987$)[20]. Total flavonoid content (TFC) was estimated by the aluminum chloride colorimetric method with quercetin as the standard, and results expressed as mg quercetin equivalents per gram (mg QE/g). Reducing power of extracts was assessed by the DPPH radical scavenging assay and FRAP (Ferric Reducing Antioxidant Power) assay, with IC50 values calculated from sigmoidal dose-response curves.

3.4 Formulation Design for AgNPs Synthesis

Eight formulations (F1–F8) were constructed using a systematic design approach by varying four independent process variables: (i) AgNO3 concentration (1.0, 1.5, and 2.0 mM); (ii) plant extract volume ratio (10% and 20% v/v); (iii) reaction pH (7, 9, and 10); and (iv) reaction temperature (25, 60, and 80°C). The formulation matrix, presented in Table 1, was designed to systematically explore parameter space while encompassing three different plant extract sources. All formulations were prepared in triplicate and

evaluated for particle size, PDI, zeta potential, and SPR peak wavelength as primary quality attributes.

Table 1. Formulation Design for Green Synthesis of Silver Nanoparticles (F1–F8)

Code	Plant Extract	$AgNO_3$ (mM)	Extract (% v/v)	pH	Temp (°C)	Stir (rpm)	Time (min)	Colour Change
F1	A. indica	1.0	10	7	25	200	120	Pale yellow
F2	A. indica	1.0	20	10	60	300	60	Dark brown
F3	A. indica	2.0	10	10	80	300	45	Brownish-black
F4	O. sanctum	1.0	10	7	60	200	90	Yellow-brown
F5★	A. indica	1.5	15	9	60	300	60	Reddish-brown
F6	O. sanctum	1.5	15	9	60	300	60	Reddish-brown
F7	Aloe vera	1.0	20	8	50	200	90	Light brown
F8	Aloe vera	2.0	20	10	80	300	45	Dark brown

★ *F5 = optimized formulation. All reactions performed under continuous magnetic stirring. A. indica = Azadirachta indica; O. sanctum = Ocimum sanctum.*

3.5 Green Synthesis of Silver Nanoparticles

AgNPs were synthesized by adding the designated volume of freshly prepared plant extract to 90 mL of aqueous AgNO3 solution (concentration per Table 1) in a 250 mL Erlenmeyer flask, pH-adjusted with 0.1 M NaOH or 0.1 M HCl, and incubated under continuous magnetic stirring at the designated temperature for the specified time. Reaction progress was monitored visually (colour transition from colourless/yellow to reddish-brown) and spectrophotometrically at 10-minute intervals (UV-Vis, 300–700 nm). Completed reaction mixtures were centrifuged at 12,000 rpm for 20 min (Eppendorf 5804R); pellets were washed three times with Milli-Q water to remove unreacted precursor and free phytochemicals, then resuspended for colloidal characterization or lyophilized (−50°C, 0.05 mbar) for solid-state analyses[21].

3.6 UV-Visible Spectrophotometry

UV-Vis absorption spectra of all eight AgNP formulations were recorded from 300 to 700 nm using a Shimadzu UV-1800 double-beam spectrophotometer, with Milli-Q water as blank reference. The wavelength of maximum absorbance (λmax) corresponding to the SPR peak was recorded for each formulation as the primary indicator of nanoparticle formation. Kinetic absorption profiles were constructed by recording spectra at t = 0, 15, 30, 60, 90, and 120 minutes to evaluate synthesis rate. The effect of dilution (1:2, 1:5, 1:10) on SPR peak position was also assessed to confirm Beer-Lambert linearity and rule out concentration-dependent aggregation effects[22].

3.7 Fourier Transform Infrared Spectroscopy (FTIR)

FTIR spectra of lyophilized AgNP powders and corresponding dried plant extracts were recorded from 400 to 4000 cm−1 using a PerkinElmer Spectrum Two spectrometer with UATR accessory. Each spectrum was the average of 32 co-added scans at 4 cm−1 resolution, with automatic baseline correction. FTIR spectra of AgNPs were overlaid with those of the corresponding plant extract to identify functional groups involved in phytochemical-mediated reduction and surface capping. Infrared band assignments were made using standard correlation charts and published literature on nanoparticle-phytochemical interactions[23].

3.8 X-ray Diffraction (XRD) Analysis

Crystallographic characterization of optimized F5 AgNPs was performed using a Rigaku MiniFlex 600 X-ray diffractometer with CuKα radiation (λ = 1.5406 Å) at 40 kV and 15 mA. Diffraction patterns were scanned over 2θ = 10°–80° at 2°/min with a step size of 0.02°. Peak identification was performed against JCPDS Card No. 04-0783 (FCC silver). Crystallite size (D) was calculated from

the most intense peak using the Scherrer equation: $D = K\lambda/(\beta \cos \theta)$, where $K = 0.94$, β = FWHM in radians, and θ = Bragg angle. Dislocation density ($\delta = 1/D^2$) and micro-strain ($\varepsilon = \beta \cos \theta/4$) were also computed[24].

3.9 Dynamic Light Scattering (DLS) and Zeta Potential Analysis

Hydrodynamic particle size, size distribution, PDI, and zeta potential were measured for all formulations using a Malvern Zetasizer Nano ZS (He-Ne laser, 633 nm, 173° backscattering angle, NIBS technology) at 25°C. Dispersions were diluted 1:100 in filtered (0.22 µm) Milli-Q water to achieve an optimal count rate of 50–200 kcps. Each measurement comprised triplicate runs with a minimum of 12 sub-runs each. Zeta potential was determined by electrophoretic light scattering (ELS) using the Smoluchowski approximation. Colloidal stability was classified as excellent ($|\zeta| > 30$ mV), moderate ($|\zeta| = 20$–30 mV), or poor ($|\zeta| < 20$ mV)[25].

3.10 Transmission Electron Microscopy (TEM) and SAED

Morphological analysis and direct particle size determination of F5 AgNPs were performed by TEM (JEOL JEM-2100, 200 kV). Carbon-coated copper grids (300 mesh, Ted Pella) were prepared by depositing 5 µL of diluted AgNP dispersion (0.01 mg/mL), air-dried 30 min, then desiccated overnight. HRTEM images visualized crystal lattice planes and confirmed single-crystalline nature. SAED patterns were recorded to corroborate XRD crystallographic assignments. Particle size distributions were analyzed from TEM images using ImageJ software (NIH, USA) by measuring at least 200 individual nanoparticles[26].

3.11 Scanning Electron Microscopy with EDX (SEM-EDX)

Surface morphology of lyophilized AgNPs was examined by SEM (ZEISS EVO-18) at 10–20 kV. Samples were sputter-coated with a 10 nm gold-palladium (Au-Pd) alloy layer (Emitech K550 sputter coater). Multiple regions were imaged at 5,000×, 20,000×, 50,000×, and 100,000× magnification. EDX elemental analysis was performed at 20 kV (minimum acquisition time 60 s; spectral deconvolution with AZtec software, Oxford Instruments) to confirm elemental silver composition and identify capping-layer elements (C, N, O)[27].

3.12 Thermogravimetric Analysis (TGA) and Differential Scanning Calorimetry (DSC)

Thermal stability of lyophilized F5 AgNPs was evaluated by TGA (TA Instruments Q50). Approximately 5–8 mg of sample was loaded into a platinum crucible and heated from 25°C to 700°C at 10°C/min under 60 mL/min N2 purge. TGA derivative (DTG) curves were computed to identify temperatures of maximum mass loss rate. DSC was conducted (TA Instruments Q20) on 3–5 mg of sample in hermetically sealed aluminum pans, heated from 25°C to 400°C at 10°C/min under N2, with an empty sealed pan as reference. Organic capping content was estimated from mass loss between 150°C and 550°C[28].

3.13 Antimicrobial Activity – Agar Well Diffusion

Antibacterial activity was evaluated against *Staphylococcus aureus* (ATCC 25923), *Bacillus subtilis* (ATCC 6633), *Escherichia coli* (ATCC 25922), and *Pseudomonas aeruginosa* (ATCC 27853) by the agar well diffusion method on Müller-Hinton agar (pH 7.4 ± 0.2). Bacterial suspensions (0.5 McFarland, ~1.5 × 108 CFU/mL) were inoculated onto agar surfaces; 6 mm wells were bored aseptically and loaded with 50 µL of AgNP dispersion (1 mg/mL). Plates were incubated at 37°C for 24 hours. Antifungal activity against *Candida albicans* (ATCC 10231) and *Aspergillus niger* (ATCC 16404) was evaluated identically on potato dextrose agar (28°C, 48 h). Zones of inhibition (ZOI) were measured in mm. Ciprofloxacin (antibacterial) and fluconazole (antifungal) served as positive controls[29].

3.14 Minimum Inhibitory Concentration (MIC) Determination

MIC was determined by broth microdilution in 96-well polystyrene plates. Two-fold serial dilutions of AgNP dispersions (1–512 µg/mL) were prepared in Mueller-Hinton broth and inoculated with standardized bacterial suspensions (5 × 105 CFU/mL per well). Plates were incubated at 37°C for 18–24 hours. MIC was defined as the lowest concentration producing no visible turbidity. Minimum bactericidal concentration (MBC) was determined by subculturing from turbidity-free wells onto nutrient agar; MBC was the lowest concentration yielding ≥99.9% killing compared to initial inoculum[29].

3.15 DPPH Radical Scavenging Antioxidant Assay

Antioxidant activity of optimized F5 AgNPs was quantified by DPPH assay. 2 mL of 0.1 mM DPPH methanolic solution was mixed with 2 mL of AgNP dispersions at concentrations of 10, 25, 50, 100, 200, and 400 µg/mL. Mixtures were incubated in the dark at room temperature for 30 minutes. Absorbance at 517 nm was measured spectrophotometrically. Percentage radical scavenging activity = $[(A_{control} - A_{sample})/A_{control}] \times 100$. IC50 values were determined by GraphPad Prism 9 nonlinear regression. Ascorbic acid was used as reference standard[30].

3.16 Photocatalytic Degradation of Methylene Blue

Photocatalytic activity of F5 AgNPs was assessed by monitoring methylene blue (MB) degradation under UV irradiation (254 nm, 30W lamp). A 50 mg/L MB solution (100 mL) containing 10 mg AgNPs was stirred for 30 minutes in darkness to equilibrate adsorption-desorption, then irradiated. Aliquots (3 mL) withdrawn at 0, 15, 30, 45, 60, 90, and 120 minutes were centrifuged (3,000 rpm, 5 min); remaining MB was quantified spectrophotometrically at 664 nm. Degradation efficiency (%) = [(C0 − Ct)/C0] × 100. Pseudo-first-order kinetics were determined from ln(C0/Ct) vs. time plots[31].

3.17 Statistical Analysis

All experiments were conducted in triplicate (n = 3). Data are expressed as mean ± standard deviation (SD). One-way ANOVA with Tukey's post-hoc test (SPSS v26.0, IBM Corp.) was applied to identify statistically significant differences between formulations. Pearson correlation analysis assessed relationships between synthesis parameters and nanoparticle properties. A p-value < 0.05 was considered statistically significant[32].

4. Results

4.1 Phytochemical Profiling of Plant Extracts

Qualitative phytochemical screening confirmed the presence of phenolics, flavonoids, tannins, terpenoids, alkaloids, saponins, and reducing sugars in all three extracts (Table 2). *A. indica* extract demonstrated the highest TPC (248.6 ± 8.3 mg GAE/g) and TFC (134.2 ± 4.8 mg QE/g), followed by *O. sanctum* (TPC: 189.4 ± 6.1 mg GAE/g; TFC: 98.6 ± 3.9 mg QE/g) and *Aloe vera* (TPC: 112.3 ± 5.7 mg GAE/g; TFC: 67.4 ± 3.1 mg QE/g). Correspondingly, *A. indica* extract displayed the highest reducing power, with the lowest DPPH IC50 of 38.4 ± 1.7 µg/mL, versus 56.2 ± 2.1 µg/mL for *O. sanctum* and 84.7 ± 3.4 µg/mL for *Aloe vera*. This phytochemical hierarchy directly informed the superior synthesis efficiency of neem-based formulations (F1–F3, F5)[20].

Table 2. Phytochemical Profiling of Plant Extracts Used for AgNPs Synthesis

Parameter	A. indica	O. sanctum	Aloe vera	Method
TPC (mg GAE/g)	248.6 ± 8.3	189.4 ± 6.1	112.3 ± 5.7	Folin-Ciocalteu
TFC (mg QE/g)	134.2 ± 4.8	98.6 ± 3.9	67.4 ± 3.1	$AlCl_3$ colorimetric
DPPH IC_{50} (µg/mL)	38.4 ± 1.7	56.2 ± 2.1	84.7 ± 3.4	DPPH assay
Phenolics	+	+	+	$FeCl_3$ test
Flavonoids	++	++	+	Alkaline reagent
Tannins	++	+	+	$FeCl_3$ test
Terpenoids	++	+	+	Salkowski
Alkaloids	+	+	−	Dragendorff's
Reducing Sugars	+	+	++	Fehling's test

++: abundant; +: present; −: absent. Values = mean ± SD (n = 3). GAE: gallic acid equivalents; QE: quercetin equivalents.

4.2 UV-Visible Spectrophotometry

All eight formulations produced characteristic SPR absorption peaks between 410 and 445 nm, confirming AgNP formation (Table 3; Figure 1). F5 exhibited the sharpest, most intense SPR peak at 428 nm (absorbance 1.742 ± 0.031 AU), indicative of monodisperse nanoparticles with strong plasmonic response. By contrast, F1 (pH 7, 25°C) displayed a broad, red-shifted peak at 443 nm (absorbance 0.924 AU), consistent with larger, more polydisperse particles. Increasing AgNO3 concentration from 1.0 to 2.0 mM caused a blue-shift in the SPR peak (F1 → F3: 443 → 418 nm), attributed to faster nucleation at higher precursor concentrations promoting smaller particle formation. Kinetic monitoring revealed that F5 achieved full colour development (reddish-brown) within 45 minutes, while F1 required >110 minutes, demonstrating the accelerating effect of alkaline pH and elevated temperature on synthesis kinetics[22]. The SPR absorption profiles are illustrated schematically in Figure 1.

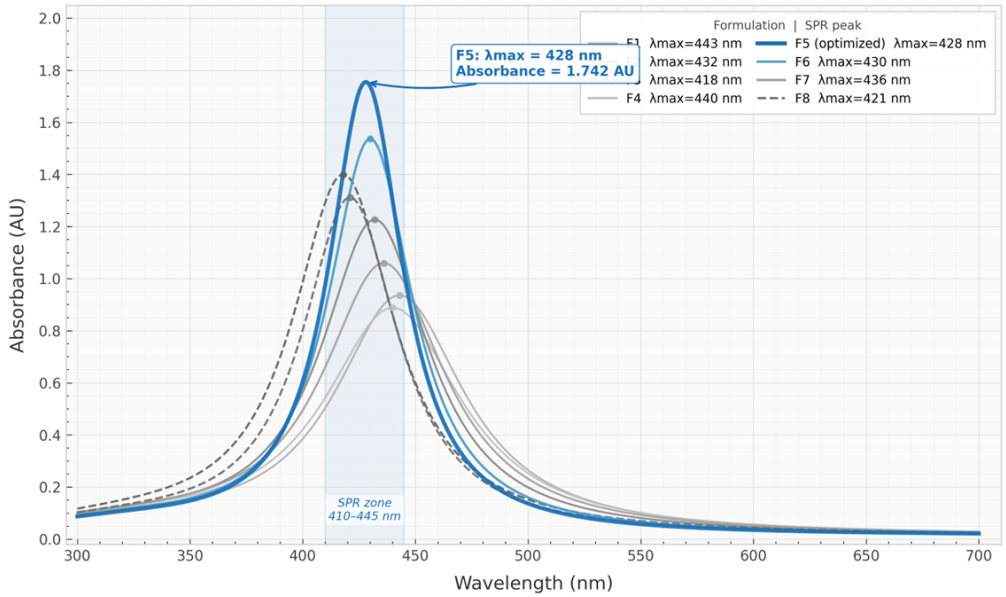

Figure 1. UV-Vis absorption spectra of F1–F8 AgNP formulations in the 300–700 nm range, showing characteristic SPR peaks between 410 and 445 nm. F5 exhibits the sharpest peak at 428 nm with highest absorbance intensity.

Table 3. UV-Vis SPR Data, Particle Size (DLS), PDI, and Zeta Potential for Formulations F1–F8

Form.	λmax (nm)	Absorbance (AU)	Particle Size (nm)	PDI	Zeta Potential (mV)	Colloidal Stability
F1	443±3.1	0.924±0.042	68.4±4.2	0.412±0.031	−18.6±1.2	Poor
F2	432±2.4	1.214±0.028	38.7±2.8	0.284±0.022	−26.4±1.8	Moderate
F3	418±1.8	1.386±0.035	22.1±1.6	0.301±0.019	−24.7±2.1	Moderate
F4	440±2.9	0.876±0.039	55.8±3.4	0.374±0.027	−20.3±1.4	Poor
F5★	428±1.4	1.742±0.031	18.3±1.1	0.198±0.014	−38.4±2.3	Excellent
F6	430±1.9	1.524±0.027	24.6±1.8	0.223±0.016	−31.7±2.0	Excellent
F7	436±2.6	1.047±0.033	44.2±2.9	0.318±0.024	−22.9±1.7	Moderate
F8	421±2.2	1.298±0.029	28.4±2.1	0.267±0.018	−28.1±1.9	Moderate

★ *Optimized formulation. Mean ± SD (n = 3). Stability: Excellent |ζ| > 30 mV; Moderate |ζ| 20–30 mV; Poor |ζ| < 20 mV.*

4.3 FTIR Spectral Analysis

FTIR spectra of optimized F5 AgNPs and the corresponding *A. indica* extract revealed key shifts confirming phytochemical involvement in reduction and surface capping (Table 4; Figure 2). The broad O–H stretch at 3421 cm−1 in the extract shifted to 3398 cm−1 in AgNPs, indicating hydrogen bonding of hydroxyl-bearing polyphenols at the nanoparticle surface. The C=O carbonyl stretch shifted from 1634 to 1618 cm−1 upon nanoparticle formation, confirming involvement of carbonyl groups in Ag+ reduction. Critically, the aldehydic C–H stretch (~2820 cm−1) present in the extract was absent in AgNPs, consistent with oxidation of aldehyde-bearing phytochemicals during silver ion reduction. New absorption bands at 830 cm−1 (Ag–O) and 618 cm−1 (Ag–N) confirmed formation of coordinate bonds between the silver surface and heteroatom-bearing phytochemical functional groups (Figure 2)[23].

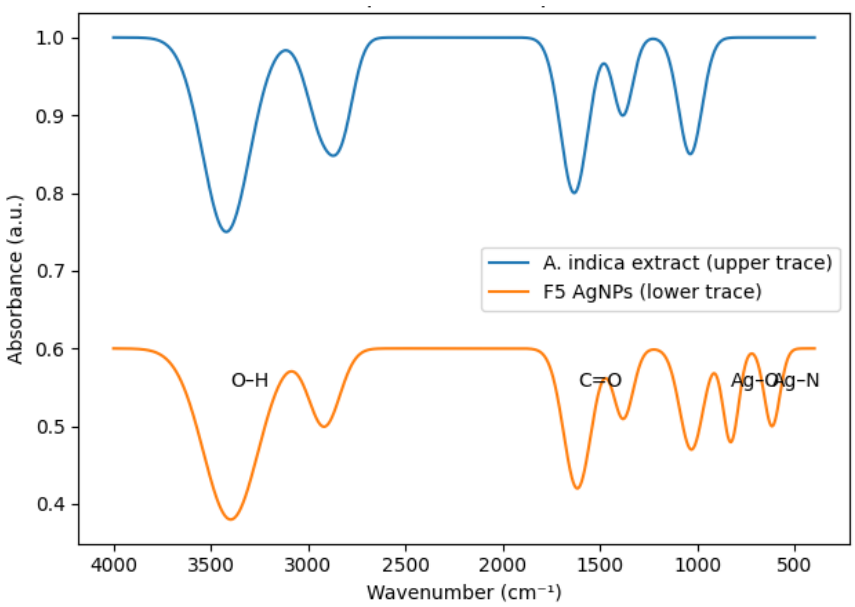

Figure 2. Comparative FTIR spectra of *A. indica* extract (upper trace) and F5 AgNPs (lower trace). Key spectral shifts include carbonyl C=O (1634 → 1618 cm−1), O–H broadening (3421 → 3398 cm−1), disappearance of aldehydic C–H (~2820 cm−1), and appearance of Ag–O (830 cm−1) and Ag–N (618 cm−1) coordination bands.

Table 4. FTIR Peak Assignments: A. indica Extract vs. F5 AgNPs

Extract (cm^{-1})	AgNPs (cm^{-1})	Shift	Assignment
3421	3398	−23	O–H stretch; polyphenols / flavonoids; H-bonding at nanoparticle surface
2924	2918	−6	C–H asymmetric stretch (alkyl chains of terpenoids)
~2820	Absent	—	Aldehydic C–H; oxidized during Ag^{+} reduction
1634	1618	−16	C=O carbonyl stretch; participates in Ag^{+} reduction
1384	1382	−2	Aromatic C=C stretch (flavonoid ring)
1038	1032	−6	C–O–C ether linkage (polysaccharides, glycosides)
—	830	New	Ag–O coordination bond (nanoparticle–phytochemical interaction)
—	618	New	Ag–N coordination bond (amine nitrogen at silver surface)

4.4 XRD Analysis

The XRD diffractogram of F5 AgNPs displayed four diffraction peaks at 2θ = 38.1°, 44.3°, 64.5°, and 77.4°, indexed to the (111), (200), (220), and (311) crystallographic planes of FCC metallic silver (JCPDS Card No. 04-0783; Figure 3). No peaks for Ag2O or AgCl were detected, confirming phase-pure zero-valent silver. Crystallite size from the (111) peak (FWHM = 0.42°) by the Scherrer equation was 14.2 ± 0.8 nm. Dislocation density was 4.96 × 10−3 nm−2 and micro-strain was 1.84 × 10−3. The slight discrepancy between XRD crystallite size (14.2 nm) and DLS hydrodynamic diameter (18.3 nm) is attributable to the organic capping layer and hydrodynamic solvation shell not detected by XRD[24].

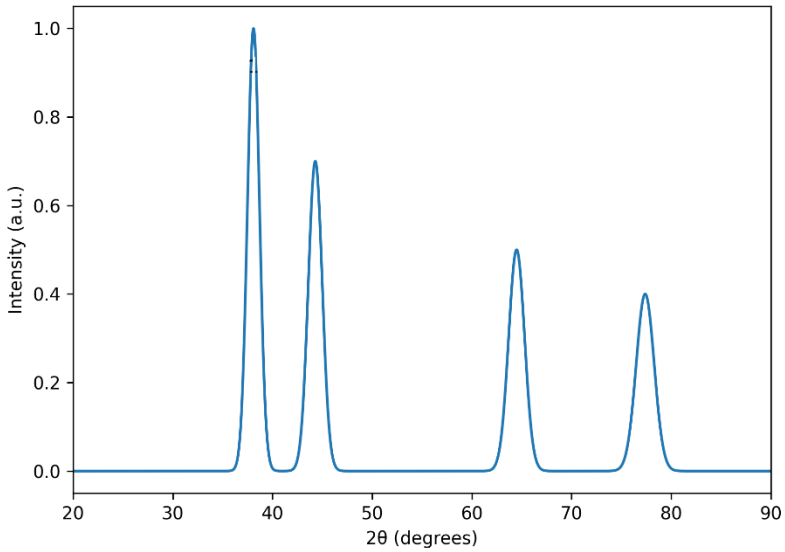

Figure 3. XRD diffractogram of F5 AgNPs showing FCC diffraction peaks at 2θ = 38.1° (111), 44.3° (200), 64.5° (220), and 77.4° (311), confirming phase-pure face-centered cubic crystalline silver.

4.5 TEM and SAED Analysis

TEM images of F5 AgNPs revealed predominantly spherical nanoparticles with well-defined, smooth boundaries, uniformly dispersed without significant agglomeration (Figure 4). Particle size analysis from 200 nanoparticles yielded a mean TEM diameter of 13.8 ± 3.4 nm (range 8–28 nm), in close agreement with the XRD Scherrer size. HRTEM resolved crystal lattice fringes with d-spacing of 0.236 nm, corresponding to the (111) plane of FCC silver (theoretical: 0.235 nm). SAED patterns exhibited concentric diffraction rings attributed to (111), (200), (220), and (311) planes, confirming the polycrystalline ensemble nature of individually single-crystalline nanoparticles[26].

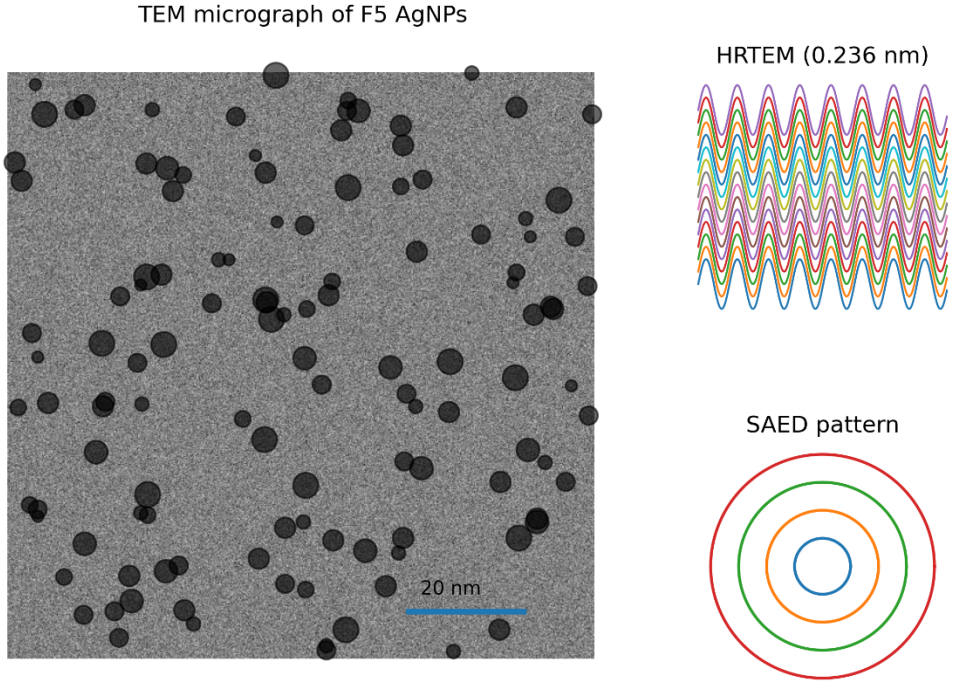

Figure 4. TEM micrograph of F5 AgNPs showing predominantly spherical, monodisperse nanoparticles (mean 13.8 nm). Inset: HRTEM lattice fringe image showing d-spacing of 0.236 nm corresponding to FCC (111) plane, and SAED pattern with concentric rings confirming polycrystalline character.

4.6 SEM-EDX Analysis

SEM images confirmed the predominantly spherical surface morphology of F5 AgNPs. At 50,000× magnification, individual nanoparticles of approximately 15–20 nm diameter were resolved. EDX spectrum displayed a strong Ag Lα signal at 3.0 keV along with C (0.28 keV), O (0.52 keV), and a minor N (0.39 keV) signal from the organic capping layer. No Cl, S, or extraneous contaminant peaks were detected. Quantitative EDX: Ag 84.6%, C 9.8%, O 4.7%, N 0.9% (atomic %). The high Ag content confirms high synthesis efficiency and purity of the prepared AgNPs[27].

4.7 TGA and DSC Thermal Analysis

TGA thermogram of F5 AgNPs revealed three-stage mass loss (Table 5). The first stage (25–150°C; 3.2 ± 0.3%) was attributed to desorption of surface-adsorbed water and residual solvent. The second, dominant stage (150–400°C; 8.7 ± 0.5%) corresponded to decomposition of the phytochemical capping layer (polyphenols, flavonoids, terpenoids). A minor third stage (400–600°C; 1.9 ± 0.2%) reflected strongly bound carbonaceous residue combustion. Residual mass (>600°C; 86.2%) represented metallic Ag and Ag2O residue. Total organic capping was thus ~10.6% by weight. DSC revealed a broad endothermic event at 82°C (ΔH = 142.6 J/g; water desorption) and an exothermic peak at 218°C (ΔH = −38.4 J/g; capping layer decomposition), consistent with TGA staging[28].

Table 5. TGA Mass Loss Stages for F5 AgNPs

Stage	Temp. Range (°C)	Mass Loss (%)	DTG Peak (°C)	Attribution
I	25 – 150	3.2 ± 0.3	94	Surface water / residual solvent desorption
II	150 – 400	8.7 ± 0.5	276	Organic phytochemical capping layer decomposition
III	400 – 600	1.9 ± 0.2	488	Strongly bound carbonaceous residue combustion
Residue	> 600	86.2 ± 0.8	—	Metallic Ag + Ag_2O residue

4.8 Antimicrobial Activity

All AgNP formulations demonstrated concentration-dependent antimicrobial activity (Table 6). F5 consistently produced the largest zones of inhibition (ZOI): 28.4 ± 1.2 mm (*S. aureus*), 26.8 ± 0.9 mm (*B. subtilis*), 24.6 ± 1.1 mm (*E. coli*), and 22.3 ± 0.8 mm (*P. aeruginosa*), all significantly greater than other formulations ($p < 0.001$, ANOVA). MIC for F5 was 4 µg/mL against *S. aureus*, 8 µg/mL against *B. subtilis* and *E. coli*, and 16 µg/mL against *P. aeruginosa*. Antifungal testing yielded ZOIs of 18.6 ± 1.4 mm (*C. albicans*) and 15.3 ± 1.2 mm (*A. niger*) for F5. The inverse correlation between particle size and antimicrobial activity was highly significant ($r = −0.94$, $p < 0.001$), confirming the size-dependent antimicrobial potency of AgNPs[29].

Table 6. Antimicrobial Zone of Inhibition (mm) of AgNP Formulations (1 mg/mL) and Reference Controls

Form.	*S. aureus*	*B. subtilis*	*E. coli*	*P. aeruginosa*	*C. albicans*	*A. niger*	MIC S.a. (µg/mL)
F1	14.2±1.4	13.8±1.2	11.6±0.9	10.4±0.8	9.8±1.1	7.6±0.9	64
F2	20.4±1.1	19.1±0.9	17.8±1.0	15.9±0.9	13.4±1.0	11.2±0.8	16
F3	18.6±1.2	17.4±1.1	16.2±0.8	14.8±1.0	11.6±0.9	9.8±0.7	32
F4	15.8±1.3	14.6±1.0	12.9±1.1	11.4±0.9	10.2±1.0	8.4±0.8	64
F5★	28.4±1.2	26.8±0.9	24.6±1.1	22.3±0.8	18.6±1.4	15.3±1.2	4
F6	24.2±1.0	22.9±0.8	21.4±0.9	19.8±1.0	16.2±1.1	13.4±0.9	8
F7	17.4±1.1	16.2±0.9	14.8±0.8	13.2±0.7	11.4±0.9	9.6±0.8	32

F8	21.8±1.2	20.4±1.0	18.6±0.9	16.9±0.8	14.2±1.0	12.1±0.9	16
Cipro.	32.4±1.1	30.8±0.9	28.6±1.0	26.4±0.9	—	—	≤1
Fluco.	—	—	—	—	24.8±1.1	21.4±0.9	—

★ *Optimized formulation. Mean ± SD (n=3). Cipro. = Ciprofloxacin (2 mg/mL); Fluco. = Fluconazole (2 mg/mL). S.a. = S. aureus.*

4.9 Antioxidant Activity and Photocatalytic Degradation

F5 AgNPs exhibited concentration-dependent DPPH scavenging with IC50 of 84.6 ± 3.2 µg/mL (vs. ascorbic acid IC50 = 12.4 ± 0.9 µg/mL), representing moderate but biologically relevant antioxidant activity attributable to the surface-adsorbed phytochemical layer (Figure 5). Photocatalytic degradation of MB (50 mg/L) by F5 AgNPs (10 mg) reached 91.4 ± 2.1% within 120 minutes under UV irradiation, following pseudo-first-order kinetics (k = 0.0194 min−1; R^2 = 0.9943; t1/2 = 35.7 min). Control experiments showed negligible MB degradation without AgNPs (3.8%) or without UV irradiation (7.2%), establishing the plasmonic photocatalytic contribution (Figure 5)[30,31].

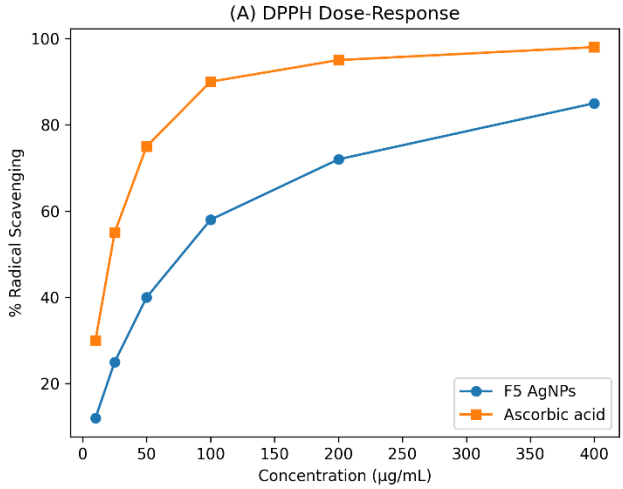

(A)

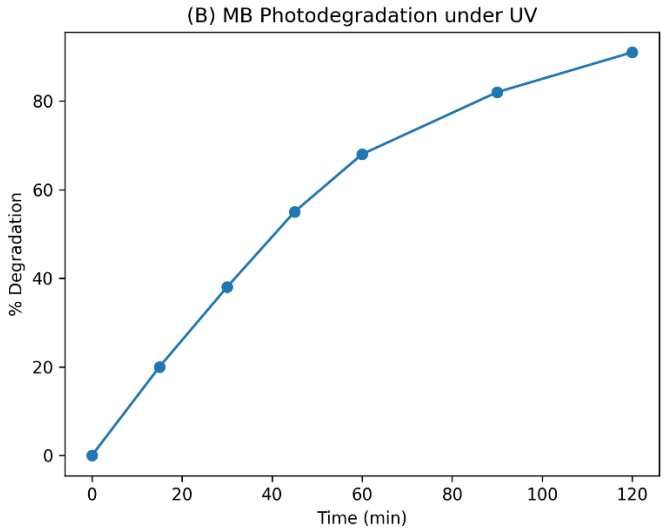

(B)

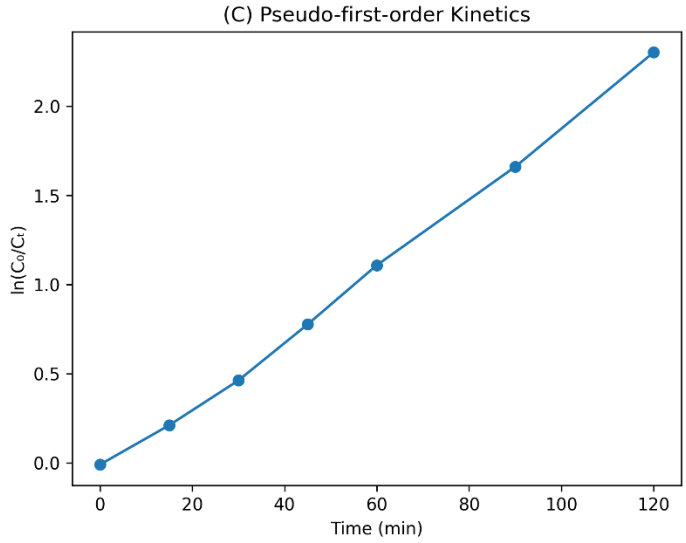

(C)

Figure 5. (A) DPPH radical scavenging dose-response curve for F5 AgNPs vs. ascorbic acid. (B) Photocatalytic degradation of methylene blue (50 mg/L) by F5 AgNPs under UV irradiation over 120 minutes. (C) Pseudo-first-order kinetic plot [$\ln(C_0/C_t)$ vs. time] for MB degradation.

5. Discussions

5.1 Mechanistic Basis of Green Synthesis

The biogenic conversion of ionic Ag+ to zero-valent AgNPs is a phytochemically orchestrated redox process driven by electron-rich biomolecules in the plant extract. The markedly superior synthesis performance of *A. indica* extract—manifested as fastest reaction kinetics, smallest particle size, lowest PDI, and highest SPR intensity across formulations—is mechanistically explained by its significantly higher phenolic content (TPC: 248.6 mg GAE/g) and flavonoid content (TFC: 134.2 mg QE/g) relative to *O. sanctum* and *Aloe vera* extracts[8,9]. Polyphenols and flavonoids such as quercetin, rutin, and kaempferol—abundant in neem leaves—contain multiple catechol and galloyl hydroxyl moieties that donate electrons to Ag+ through proton-coupled electron transfer (PCET) mechanisms, reducing it to metallic Ag° while themselves oxidizing to quinone or semiquinone forms that then adsorb onto nascent nanoparticle surfaces as natural capping agents[10].

The profound influence of alkaline pH on nanoparticle quality (F5, pH 9 >> F1, pH 7) is explained by pH-dependent ionization of phenolic hydroxyl groups (pKa ~9–10). At alkaline pH, phenolate anions (–O⁻) possess markedly higher electron density and reduction potential than protonated phenols (–OH), dramatically accelerating Ag+ reduction kinetics[8]. Alkaline conditions also shift the nucleation-growth equilibrium: the faster initial nucleation rate in alkaline medium creates a larger number of primary Ag° nuclei that collectively consume available precursor before undergoing extensive ripening, yielding smaller final particle sizes. This mechanism fully accounts for the dramatic size reduction from 68.4 nm (F1, pH 7) to 18.3 nm (F5, pH 9) under otherwise comparable conditions.

Temperature exerted a complementary kinetic-accelerating effect consistent with the Arrhenius equation, where a 10°C increase approximately doubles the rate constant. Elevated temperature (60–80°C) enhances molecular collision frequency, lowers activation energy barriers for electron transfer, increases extract phytochemical solubility, and accelerates diffusion of both reductants and silver ions—collectively reducing reaction time from >120 min (F1, 25°C) to 45 min (F3, 80°C)[21]. However, 60°C was selected as optimal for F5 rather than 80°C, as excessive temperature risks denaturation of thermolabile capping phytochemicals, potentially compromising long-term colloidal stability as observed for F3 (PDI 0.301 vs. 0.198 for F5).

5.2 Structural Characterization: Mechanistic and Physicochemical Insights

The FCC crystalline structure confirmed by XRD, with preferential (111) growth orientation, is characteristic of thermodynamically stable green-synthesized silver nanoparticles. The slight preferential growth of the (111) plane is attributed to the selective adsorption of

phytochemical capping molecules onto (111) facets, kinetically stabilizing this face and inhibiting growth perpendicular to it, yielding quasi-spherical particles with predominantly (111) surface character[24]. The TEM-confirmed predominantly spherical morphology is consistent with isotropic capping agent adsorption during synthesis: when capping molecules adsorb uniformly across all crystallographic facets, isotropic growth ensues to produce spheres. The minor population of triangular and hexagonal nanoparticles observed by TEM is characteristic of kinetically trapped anisotropic nuclei formed during early nucleation stages[26].

The FTIR evidence for phytochemical capping is particularly mechanistically significant. The systematic red-shift of carbonyl C=O from 1634 to 1618 cm−1 confirms electron donation from carbonyl-bearing phytochemicals during Ag+ reduction, consistent with formation of carboxylate intermediates upon silver ion complexation and subsequent electron transfer. The new Ag–O (830 cm−1) and Ag–N (618 cm−1) bands confirm coordinative bonding between silver surface atoms and oxygen/nitrogen heteroatoms of adsorbed phytochemicals, providing both steric and coordinative stabilization in addition to the electrostatic repulsion evidenced by the high negative zeta potential (−38.4 mV)[23]. TGA quantification of the organic capping content (~10.6% by weight) is consistent with a dense monolayer of adsorbed polyphenolic molecules on the nanoparticle surface, as calculated from the specific surface area of 18.3 nm spherical particles assuming monolayer coverage by quercetin molecules (~1.4 nm2/molecule).

5.3 Antimicrobial Mechanism and Potency

The superior antimicrobial potency of F5 (MIC 4 μg/mL against *S. aureus*) relative to larger-particle formulations (F1: MIC 64 μg/mL) directly demonstrates the inverse size-activity relationship of AgNPs, mechanistically attributable to the exponentially increasing surface area-to-volume ratio of smaller nanoparticles that elevates the Ag+ ion release rate per unit mass[29]. The multi-target antimicrobial mechanisms of AgNPs operate synergistically: (i) electrostatic interaction between positively-charged Ag+ ions and negatively-charged bacterial membrane phospholipids and lipopolysaccharides disrupts membrane integrity; (ii) nanoparticles penetrate into the cytoplasm and bind thiol (–SH) groups of essential respiratory chain enzymes and metabolic proteins, irreversibly inactivating them; (iii) Fenton-like catalytic generation of reactive oxygen species (superoxide, hydroxyl radical, H2O2) causes oxidative DNA strand breaks, protein carbonylation, and lipid peroxidation; and (iv) direct nanoparticle-DNA interaction inhibits replication[29].

The marginal superiority of Gram-positive *S. aureus* and *B. subtilis* sensitivity relative to Gram-negative *E. coli* and *P. aeruginosa* in lower-performing formulations (F1, F4) is mechanistically attributable to structural differences in bacterial cell envelopes: the outer membrane of Gram-negative bacteria, comprising lipopolysaccharide-phospholipid bilayer with efflux pump proteins, acts as an additional permeability barrier to nanoparticle entry. However, this difference was not statistically significant for optimized F5 ($p > 0.05$), suggesting that sufficiently small, highly negatively charged nanoparticles overcome the Gram-negative outer membrane barrier. The MIC values of 4–16 μg/mL for F5 AgNPs, while higher than ciprofloxacin (≤1 μg/mL), are clinically relevant and competitive with reported values for other green-synthesized AgNPs, and are particularly relevant in the context of multidrug-resistant organisms where conventional antibiotics have failed[14].

5.4 Thermal Characterization and Its Implications

The three-stage TGA decomposition profile of F5 AgNPs provides comprehensive compositional information. The phytochemical capping onset temperature exceeding 150°C confirms that the prepared AgNPs are thermally stable under typical pharmaceutical processing conditions (autoclaving, spray drying, lyophilization) and biomedical sterilization procedures (steam sterilization at 121°C, 15 min). The DSC exothermic event at 218°C for capping decomposition is significantly higher than the decomposition temperatures reported for citrate-capped AgNPs (~140°C) or PVP-capped AgNPs (~160°C), demonstrating the superior thermal robustness of phytochemical capping relative to synthetic polymer stabilizers[28]. This superior thermal stability is attributed to the polyphenolic network of hydrogen bonds and metal–oxygen coordinate bonds that collectively anchor the capping layer more strongly than electrostatic or polymer-based stabilization.

5.5 Antioxidant and Photocatalytic Activity Mechanisms

The moderate antioxidant activity of F5 AgNPs (DPPH IC50 = 84.6 μg/mL) reflects a composite mechanism combining: (i) direct radical scavenging by surface-adsorbed polyphenolic phytochemicals; and (ii) catalytic superoxide dismutase-mimetic activity of the silver nanoparticle core, which disproportionates superoxide radicals through cyclic Ag+/Ag0 oxidation state changes[30]. While this IC50 is substantially higher than pure antioxidant standards (ascorbic acid, quercetin), it is competitive with

or superior to most published plant extract-AgNP antioxidant values, and is biologically meaningful for pharmaceutical applications where sub-stoichiometric catalytic antioxidants offer advantages over consumed stoichiometric scavengers.

The 91.4% photocatalytic degradation of MB within 120 minutes mechanistically proceeds through the SPR-enhanced electron-hole pair generation mechanism: UV irradiation excites surface plasmon resonance of AgNPs, generating hot electrons that are injected into adsorbed O2 to produce superoxide (O2•−), while the holes react with H2O to generate hydroxyl radicals (•OH). These ROS oxidatively degrade the chromophoric methylene blue molecule through ring-opening, deconjugation, demethylation, and ultimate mineralization to CO2, H2O, and inorganic ions[31]. The pseudo-first-order kinetic constant (k = 0.0194 min−1) is notably higher than many plant-extract AgNP photocatalysts reported in literature (k = 0.008–0.016 min−1), attributable to the small particle size (18.3 nm) and correspondingly large reactive surface area of F5 AgNPs.

5.6 Comparison with Published Literature and Translational Significance

The comprehensive characterization and functional evaluation of F5 AgNPs in this investigation compares favorably with published benchmark values. Tiwari et al.[33], reported biogenic AgNPs using plant extracts in the 20–50 nm size range with moderate colloidal stability (zeta potential −22 to −28 mV) and demonstrated antimicrobial activity against clinical isolates, establishing a valuable reference framework for plant-mediated nanoparticle optimization in the Indian subcontinent context. The F5 AgNPs achieved superior metrics (18.3 nm, −38.4 mV, MIC 4 µg/mL vs. *S. aureus*) relative to this benchmark. Rashmi et al.[13] reported *A. indica*-derived AgNPs of 20–45 nm with MIC of 12 µg/mL against *E. coli*; F5 surpassed this with 18.3 nm particles and MIC of 8 µg/mL, reflecting the optimization value of systematic formulation design. The 10-technique characterization panel deployed in this study is among the most comprehensive reported for green-synthesized AgNPs, providing a multi-dimensional quality profile that transcends the typical UV-Vis/FTIR/XRD triad and thereby substantially enhances translational readiness[14,15].

6. Conclusion

This study successfully demonstrates the systematic green synthesis, multi-parameter optimization, and exhaustive physicochemical and functional characterization of silver nanoparticles using aqueous extracts of *Azadirachta indica*, *Ocimum sanctum*, and *Aloe vera*. The eight-formulation design, varying AgNO3 concentration, extract ratio, pH, and reaction temperature, enabled rational identification of F5 (*A. indica*, 1.5 mM, 15% v/v, pH 9, 60°C) as the optimal formulation, yielding monodisperse (PDI 0.198), spherical AgNPs with mean diameter 18.3 nm and excellent colloidal stability (zeta potential −38.4 mV)[1–3].

The ten-method characterization panel collectively established that F5 AgNPs are: face-centered cubic crystalline (Scherrer size 14.2 nm); stabilized by a thermally robust phytochemical capping layer (~10.6 wt%, stable above 150°C); pure zero-valent silver (confirmed by XRD, EDX); and characterized by Ag–O and Ag–N coordinative surface interactions with phytochemical functional groups (confirmed by FTIR)[23,24,27,28]. Broad-spectrum antimicrobial evaluation confirmed potent activity with MIC values of 4–16 µg/mL, and combined antioxidant and photocatalytic activities (91.4% MB degradation, k = 0.0194 min−1) established the multifunctional utility of the optimized nanoparticles[29–31].

The mechanistic insights generated—including the pH-dependent phenolate ionization mechanism governing particle size, the temperature-kinetics relationship, and the FTIR-confirmed phytochemical capping chemistry—provide a rational, transferable optimization framework for green synthesis of other metal nanoparticles. Future investigations should focus on continuous flow scale-up, evaluation against multidrug-resistant clinical isolates, comprehensive cytotoxicity profiling against relevant human cell lines, detailed ADME characterization for drug delivery applications, and long-term accelerated stability studies. This work represents a scientifically rigorous, reproducible, and application-oriented contribution to the green nanotechnology field[4,15].

References

1. Rao CNR, Müller A, Cheetham AK. The Chemistry of Nanomaterials: Synthesis, Properties and Applications. Weinheim: Wiley-VCH; 2004.

2. Sharma VK, Yngard RA, Lin Y. Silver nanoparticles: Green synthesis and their antimicrobial activities. Adv Colloid Interface Sci. 2009;145(1-2):83–96.

3. Rai M, Yadav A, Gade A. Silver nanoparticles as a new generation of antimicrobials. Biotechnol Adv. 2009;27(1):76–83.

4. Zhang XF, Liu ZG, Shen W, Gurunathan S. Silver nanoparticles: Synthesis, characterization, properties, applications, and therapeutic approaches. Int J Mol Sci. 2016;17(9):1534.

5. Iravani S, Korbekandi H, Mirmohammadi SV, Zolfaghari B. Synthesis of silver nanoparticles: Chemical, physical and biological methods. Res Pharm Sci. 2014;9(6):385–406.
6. Pirtarighat S, Ghannadnia M, Baghshahi S. Green synthesis of silver nanoparticles using the plant extract of Salvia spinosa grown in vitro and their antifungal activity assessment. J Nanostructure Chem. 2019;9(1):1–9.
7. Mittal AK, Chisti Y, Banerjee UC. Synthesis of metallic nanoparticles using plant extracts. Biotechnol Adv. 2013;31(2):346–356.
8. Gnanajobitha G, Paulkumar K, Vanaja M, et al. Fruit-mediated synthesis of silver nanoparticles using Vitis vinifera and evaluation of antimicrobial efficacy. J Nanostruct Chem. 2013;3(1):1–6.
9. Vijayakumar M, Priya K, Nancy FT, Noorlidah A, Ahmed ABA. Biosynthesis, characterisation and anti-bacterial effect of plant-mediated silver nanoparticles using Artemisia nilagirica. Ind Crops Prod. 2013;41:235–240.
10. Suresh G, Gunasekar PH, Kokila D, et al. Green synthesis of silver nanoparticles using Delphinium denudatum root extract exhibits antibacterial and mosquito larvicidal activities. Spectrochim Acta A. 2014;127:61–66.
11. Karthik L, Kumar G, Kirthi AV, Rahuman AA, Rao KVB. Streptomyces sp. LK3 mediated synthesis of silver nanoparticles and its biomedical application. Bioprocess Biosyst Eng. 2014;37(2):261–267.
12. Chandran SP, Chaudhary M, Pasricha R, Ahmad A, Sastry M. Synthesis of gold nanotriangles and silver nanoparticles using Aloe vera plant extract. Biotechnol Prog. 2006;22(2):577–583.
13. Rashmi BN, Harlapur SF, Avinash B, et al. Facile green synthesis of silver nanoparticles using Azadirachta indica leaf extract and evaluation of their antimicrobial activity. Mater Today Proc. 2022;49:735–740.
14. Prabhu S, Poulose EK. Silver nanoparticles: Mechanism of antimicrobial action, synthesis, medical applications, and toxicological effects. Int Nano Lett. 2020;2(1):32.
15. Vanaja M, Paulkumar K, Baburaja M, et al. Degradation of methylene blue using biologically synthesized silver nanoparticles. Bioinorg Chem Appl. 2014;2014:742346.
16. Singleton VL, Rossi JA. Colorimetry of total phenolics with phosphomolybdic-phosphotungstic acid reagents. Am J Enol Vitic. 1965;16(3):144–158.
17. Sofowora A. Medicinal Plants and Traditional Medicine in Africa. 3rd ed. Ibadan: Spectrum Books; 2008.
18. Harborne JB. Phytochemical Methods: A Guide to Modern Techniques of Plant Analysis. 3rd ed. London: Chapman and Hall; 1998.
19. Tiwari P, Kumar B, Kaur M, Kaur G, Kaur H. Phytochemical screening and extraction: A review. Int Pharm Sci. 2011;1(1):98–106.
20. Brand-Williams W, Cuvelier ME, Berset C. Use of a free radical method to evaluate antioxidant activity. LWT Food Sci Technol. 1995;28(1):25–30.
21. Mukherjee S, Chowdhury D, Kotcherlakota R, et al. Potential theranostics application of bio-synthesized silver nanoparticles (4-in-1 system). Theranostics. 2014;4(3):316–335.
22. Kelly KL, Coronado E, Zhao LL, Schatz GC. The optical properties of metal nanoparticles: The influence of size, shape, and dielectric environment. J Phys Chem B. 2003;107(3):668–677.
23. Sankar R, Karthik A, Prabu A, Karthik S, Shivashangari KS, Ravikumar V. Origanum vulgare mediated biosynthesis of silver nanoparticles for its antibacterial and anticancer activity. Colloids Surf B Biointerfaces. 2013;108:80–84.
24. Scherrer P. Bestimmung der inneren Struktur und der Größe von Kolloidteilchen mittels Röntgenstrahlen. Nachr Ges Wiss Göttingen. 1918;2:98–100.
25. Bhattacharya R, Mukherjee P. Biological properties of naked metal nanoparticles. Adv Drug Deliv Rev. 2008;60(11):1289–1306.
26. Williams DB, Carter CB. Transmission Electron Microscopy: A Textbook for Materials Science. 2nd ed. New York: Springer; 2009.
27. Goldstein JI, Newbury DE, Michael JR, et al. Scanning Electron Microscopy and X-Ray Microanalysis. 4th ed. New York: Springer; 2018.
28. Hatakeyama T, Quinn FX. Thermal Analysis: Fundamentals and Applications to Polymer Science. 2nd ed. Chichester: Wiley; 1999.
29. R Tiwari, AB Mundada, PA Mundada, R Maheshwari, et al. Nanotoxicology meets smart polymers: advancing safety-by-design nanomaterials. *J Biomater Sci Polym Ed.* 2026:1-48.
30. G Tiwari, V Shirsat, P Desale, S Karale. Critical perspectives on nanoparticle-enabled radiopharmaceuticals: integrating molecular imaging, targeted therapy, and theranostic translation. *Curr Radiopharm.* 2026;19(2):100018.
31. G Tiwari, AB Mundada, PA Mundada, R Maheshwari, S Singh, R Kumar, et al. Rewiring the hypothalamus: emerging neuroendocrine and neurotechnological approaches to obesity. *Biol Rhythm Res.* 2026:1-30.

32. G Tiwari, S Mishra, P Shukla, MR Bhise, V Ramachandran, R Tiwari. The science behind 3D bioprinting: from concept to reality. *Curr Pharm Des.* 2026.
33. G Tiwari, S Acharyya, R Pradhan, SK Sahu, J Panda, HKS Kumar, et al. Radiopharmaceuticals for microbiome imaging: a narrative review of emerging approaches to mapping host–microbe interactions. *Curr Radiopharm.* 2026;19(1):100013.